


Fluid mechanics of blood flow in human fetal left ventricles based on patient-specific 4D ultrasound scans

Chang Quan Lai¹ · Guat Ling Lim² · Muhammad Jamil¹ · Citra Nurfarah Zaini Mattar² · Arijit Biswas² · Choon Hwai Yap¹ 

Received: 2 August 2015 / Accepted: 1 December 2015 / Published online: 16 December 2015
© Springer-Verlag Berlin Heidelberg 2015

Abstract The mechanics of intracardiac blood flow and the epigenetic influence it exerts over the heart function have been the subjects of intense research lately. Fetal intracardiac flows are especially useful for gaining insights into the development of congenital heart diseases, but have not received due attention thus far, most likely because of technical difficulties in collecting sufficient intracardiac flow data in a safe manner. Here, we circumvent such obstacles by employing 4D STIC ultrasound scans to quantify the fetal heart motion in three normal 20-week fetuses, subsequently performing 3D computational fluid dynamics simulations on the left ventricles based on these patient-specific heart movements. Analysis of the simulation results shows that there are significant differences between fetal and adult ventricular blood flows which arise because of dissimilar heart morphology, E/A ratio, diastolic–systolic duration ratio, and heart rate. The formations of ventricular vortex rings were observed for both E- and A-wave in the flow simulations. These vortices had sufficient momentum to last until the end of diastole and were responsible for generating significant wall shear stresses on the myocardial endothelium, as well as helicity in systolic outflow. Based on findings from previous studies, we hypothesized that these vortex-induced flow properties play an important role in sustaining the efficiency of diastolic

filling, systolic pumping, and cardiovascular flow in normal fetal hearts.

Keywords Cardiovascular · Left ventricular fluid mechanics · Human fetal · Computational fluid dynamics simulations

1 Introduction

Intracardiac blood flow is a key component of the cardiovascular system, the characteristics of which are crucial for a complete understanding of how the heart functions. Vortex formation during diastole, for instance, has been shown to assist ventricular filling (Martínez-Legazpi et al. 2014) and mitral valve closure (Bellhouse 1972) and possibly prevent thrombus formation (Ghosh et al. 2010). In addition, the hydrodynamic forces associated with intracardiac blood flow have been identified as an important epigenetic factor in determining the physiology and function of the heart (Groenendijk et al. 2005; Hogers et al. 1995; Hove et al. 2003; Marshall et al. 2004; Pasipoularides 2009; Tobita and Keller 2000; Tworetzky et al. 2004). This is thought to be accomplished through endocardial cells which sense the mechanical cues generated by the blood flow and cause an up- or down-regulation of gene expression (Olesen et al. 1988) that can, in turn, alter the performance or morphology of the heart. In the case of abnormal flows, a heart may therefore be readily remodeled into a form that further encourages the abnormality of the flow, leading into a vicious cycle that ends with heart developing into a diseased state (Hove et al. 2003; Pasipoularides 2009, 2012). Intracardiac blood flow is therefore useful in the investigation of the genesis of cardiac diseases.

In recent years, significant progress has been made in the mapping of time-resolved blood flows in adult and

Electronic supplementary material The online version of this article (doi:10.1007/s10237-015-0750-5) contains supplementary material, which is available to authorized users.

✉ Choon Hwai Yap
bieyapc@nus.edu.sg

¹ Department of Biomedical Engineering, National University of Singapore, Singapore, Singapore

² Department of Obstetrics and Gynecology, Yong Loo Lin School of Medicine, National University Health Systems, National University of Singapore, Singapore, Singapore

animal hearts in vivo (Elaz et al. 2014; Johnson et al. 2013; Markl et al. 2005; Wang et al. 2009; Yamashita et al. 2007). For instance, time-resolved 3D magnetic resonance imaging (MRI) has been successfully applied to provide high-resolution flow measurements in an adult left ventricle (Elaz et al. 2014; Wigström et al. 1999), aortic valve sinus (Markl et al. 2005), and carotid siphon (Yamashita et al. 2007).

In contrast, the details of intracardiac flow profiles in human fetal hearts have remained relatively obscure (Pasipoularides 2009). Because there are considerable differences between the physiology and activities of the fetal and adult cardiovascular system (e.g., E/A ratio, systole–diastole duration ratio), the conclusions drawn from the studies of adult hearts cannot be extended to fetal hearts in a straightforward manner, significantly hindering the understanding of the development of congenital heart diseases. One possible reason for this lack of data on fetal hearts could be the challenge in developing simple in vivo imaging techniques that have been proven safe for use on fetuses and yet provide sufficient time and spatial resolution for computational processing. For instance, computerized tomography (CT) scans are not deemed suitable for routine scanning of second trimester fetuses since it is an ionizing radiation, while magnetic resonance imaging requires gating to the heart rate, which is technically challenging (Holmes et al. 2008), and encounters difficulty with motion artifacts due to fetal motion, which occurs because of extended scan duration.

To circumvent these technical difficulties, we introduce, in this report, a technique for obtaining patient-specific, time-resolved 3D flow profile of fetal intracardiac flows through computational fluid dynamic (CFD) simulations. This is accomplished through the use of 4D spatiotemporal image correlation (STIC) ultrasound scans that are widely accepted for use in routine antenatal scans (Ahmed 2014). These ultrasound scans were then used to reconstruct the fetal heart in 3D for multiple time points in the cardiac cycle, thereby allowing the ventricular motion to be ascertained. Intracardiac blood flow can then be obtained through CFD simulations based on this quantified dynamic movement of the heart. The technique is demonstrated with three patient-specific normal fetal left ventricles over one full cardiac cycle, and the results of the intracardiac flow are also analyzed and elucidated in detail.

2 Methods

2.1 Subjects

The ultrasound scans were performed on three healthy fetal hearts with a gestational age of 20 weeks during routine antenatal scans. The study protocols were approved by the

Domain Specific Review Board of the National Health Group (Singapore), and written informed consent were obtained from all participants.

2.2 4D ultrasound image acquisition

Four-dimensional (3D + time) STIC ultrasound scans of the fetal hearts (shown in the four-chamber view in Fig. 1a) were carried out using GE Voluson 730 (General Electric, Connecticut, USA) with a RAB 4- to 8-L transducer (4–8.5-MHz frequency). In STIC mode, the ultrasound transducer is automatically swept over the region of interest slowly so that a large number of 2D ultrasound scans can be obtained over space and time over multiple heart beats. The images are then converted into multiple 3D volume images at different time points, via spatial and temporal correlation between images, which is guided by periodic image features of the beating heart (DeVore et al. 2003; Taddei et al. 2007). Only one cardiac cycle of volume images was produced.

In our images, the sweep occurred over 10–15 s, over 25–35 cardiac cycles. STIC imaging occurred at frame rates of 73–93 fps. Over 10–15 s of imaging, 29–37 volume images per cardiac cycle could be acquired. Based on a 5-Hz center frequency, the axial resolution was estimated to be 0.46 mm. In the out-of-plane direction, about 0.9–1.7 image frames were captured per 1 degree angle of out-of-plane sweep (0.5–0.9 mm spacing). Due to the noise, however, the ultrasound images could only be resolved with certainty to approximately 1 mm. The data were processed using the program, 4D View (General Electric, Connecticut, USA).

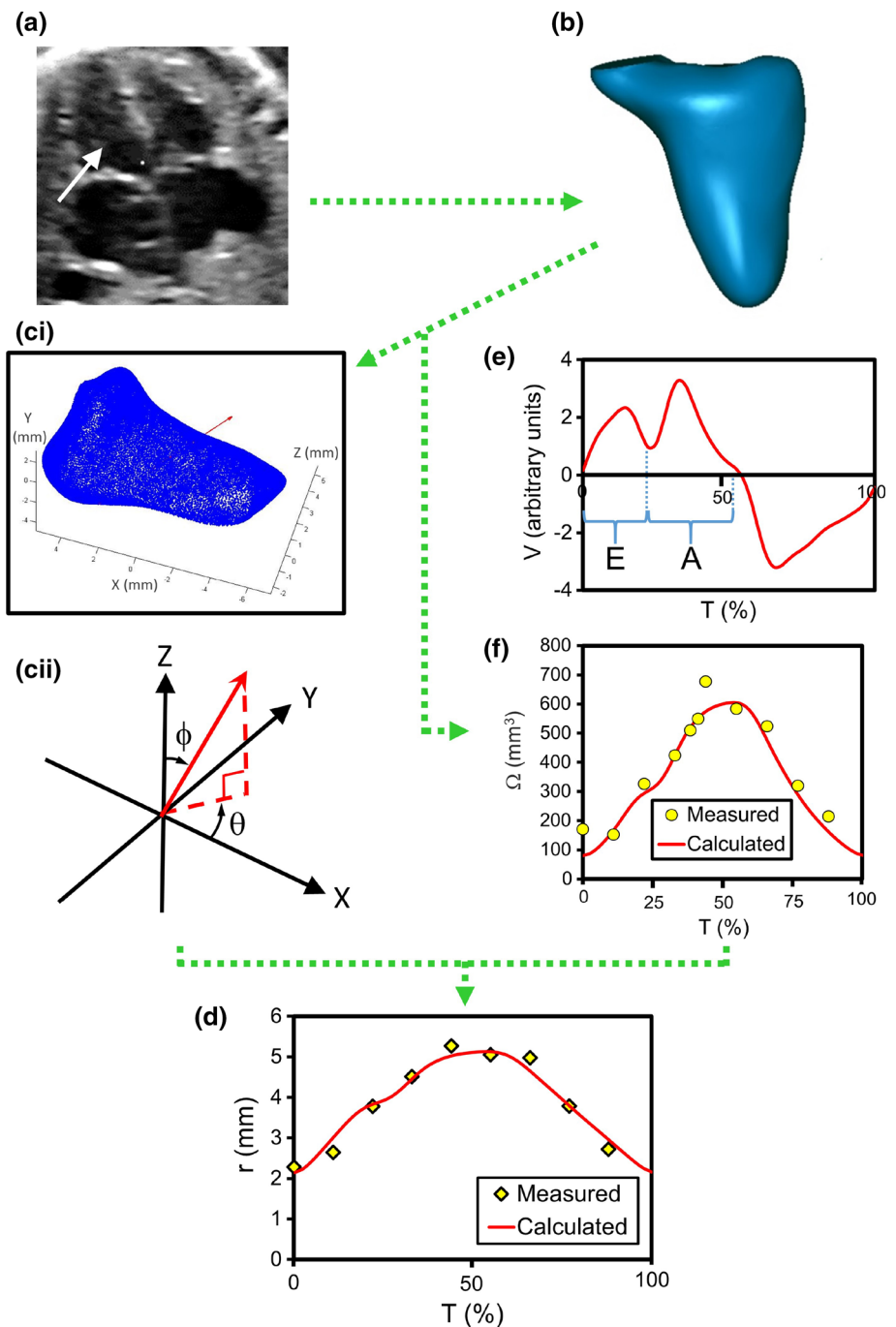
2.3 3D surface reconstruction of fetal hearts

To reconstruct the 3D left ventricles, the volume image at every time point was first exported as a stack of 29 2D image slices (maximum number of slices permitted by “4D View”), with each slice having a thickness of 0.7 mm. The thickness of the image slice was chosen such that the 29 slices covers the entire volume of the fetal heart while maximizing the out-of-plane resolution for the surface reconstruction.

Each image slice was then processed using the threshold function in Adobe Photoshop CS 6 (Adobe Systems Inc., California, USA), so that the grayscale image slices were converted into black-and-white images, with black representing the blood space in the ventricular chamber. In addition, the irrelevant space surrounding the fetal heart was erased to minimize errors introduced by noise in these regions.

The black-and-white image stack was then used to reconstruct the 3D model of the left ventricular chamber of the fetal heart (Fig. 1b) using an open-source software, Vascular Modeling Toolkit (VMTK, www.vmtk.org). Level set segmentation was performed using the ‘Colliding Fronts’ initialization option, and exported in the “.stl” format. The 3D

Fig. 1 Process flow for obtaining time-resolved 3D flows in a fetal left ventricle. **a** Representative ultrasound image obtained using 4D STIC. Left ventricle is indicated by a *white arrow*. **b** 3D surface reconstruction. **ci** Point cloud of fetal ventricular surface being probed (*red arrow* piercing through the point cloud). **cii** Coordinate system used throughout this study. **d** Measured (data points) and fitted (*line*) trend of r versus T (%) in a single direction. T refers to the period of a single cardiac cycle and T (%) refers to the fraction of the cardiac cycle expressed as a percentage. **e** Plot of inflow (positive) and outflow (negative) velocities, V , over T (%), obtained using fitting with Eq. (1). **f** Measured (data points) and fitted (*line*) trend of ventricular volume, Ω , over T (%)



surface reconstruction was carried out for 7–10 time points per cardiac cycle for each of the fetal left ventricle and smoothed.

2.4 Quantification of the ventricular wall motion

To quantify the ventricular wall motion, a spherical coordinate system was first established for each case study, 1. Using a custom MATLAB code, the reconstructed fetal left ventricle at any one time instance was imported as a point

cloud from the “.stl” file, and the quantification of the radial distance between the ventricular wall and the origin was carried out for 614 directions (Fig. 1ci). The directions were obtained by systematically varying the probing directions from 0° to 170° for θ and 0° to 350° for ϕ in intervals of 10° (see Fig. 1cii for an illustration of the coordinate system used in this study), which provides comprehensive coverage of the model surface without overlap.

By repeating this over all time points, we obtained the distance between the boundary of the ventricle and the arbitrary

rary center, $r(\theta, \phi, t)$, as a function of the two spherical coordinates and time. An example of the r versus t data for a particular direction obtained this way is plotted as points in Fig. 1d.

We then sought a mathematical model to describe the variation of r versus t in all directions by fitting a periodic trend line to the data points. To do so, we start with a clinical measurement of the pulsed Doppler waveform from the literature (Godfrey et al. 2012) that describes the velocity of blood passing through the mitral valve opening and the left ventricular outflow tract (LVOT). The inflow into the left ventricle is denoted as positive and outflow as negative. To convert these waveforms to volume waveforms, we need to account for any mismatch between inflow cross-sectional area and outflow cross-sectional area. This is done by scaling positive velocity-time integral to be equal to the negative velocity-time integral, such that a characteristic volume inflow/outflow rate curve can be plotted (Fig. 1e). This characteristic curve can now be scaled up/down to fit measured ventricular volume data and act as a boundary condition to the simulated ventricular volume. The first hump during diastole represents the E-wave (inflow due to the suction provided by the expansion of the left ventricle) and the second hump represents the A-wave (inflow due to the squeezing action of the left atrium, also known as ‘atrial kick’). This characteristic volume flow rate versus time waveform, $V(t)$, can be described by a Fourier function with eight frequency components (total of 17 terms):

$$V(t) = a_0 + \sum_{i=1}^8 [a_i \cos(i\omega t) + b_i \sin(i\omega t)] \quad (1)$$

ω refers to the angular velocity and is given by $2\pi/T$ where T is the period of one cardiac cycle. The terms a_i and b_i are the fitting parameters and are constants. An example of Eq. (1) can be seen in Fig. 1e.

Integrating Eq. (1) with respect to time then gives the characteristic volume versus time relationship, which could be subsequently fitted to the volumes measured from the reconstructed 3D models of the fetal left ventricle (Fig. 1f). The characteristic volume versus time curve of the ventricle, Ω , can be expressed as:

$$\Omega(t) = A \int V(t) dt + C \quad (2)$$

where A and C are the fitting parameters. Note that the area of flow had been incorporated into A .

Since the volume of a sphere is proportional to r^3 , we can model $r(\theta, \phi, t)$ as a function of the third root of Ω :

$$r(\theta, \phi, t) = \alpha(\theta, \phi) [\Omega(t)]^{\frac{1}{3}} + \kappa(\theta, \phi) \quad (3)$$

where $\alpha(\theta, \phi)$ and $\kappa(\theta, \phi)$ can be obtained through a surface fitting of the values of α (or κ) versus θ and ϕ using a polynomial function up to the fifth degree for θ and ϕ (i.e., highest order terms are θ^5 , ϕ^5 and $\theta^5\phi^5$) in MATLAB. α describes the amplitude of the periodic waveform Ω , while κ describes the initial condition of r . The values of α and κ at every spatial point on the ventricle can be found using the measured $r(\theta, \phi, t)$ data. A sample of fitting this model to r versus t data is shown in Fig. 1d. Because the ends of the polynomial fit may not match each other (e.g., $\alpha(\theta, 0^\circ) \neq \alpha(\theta, 360^\circ)$ even though they have effectively the same angle coordinates), linear interpolation was employed in the affected regions to ensure that the model retained a smooth and closed surface during the simulated diastole and systole.

2.5 CFD simulations

CFD meshing and simulations were performed with ANSYS Workbench and FLUENT 15.0 (ANSYS, Inc., Canonsburg, PA, USA) respectively. A single 3D mesh of the fetal left ventricle from a particular time instance was input to FLUENT. A user-defined function (UDF) was employed to dictate the ventricular motion in the CFD simulations. Between time steps, the UDF updates surface nodes, with a position vector of R , using a factor, f , so that

$$R_{t+\Delta t} = fR_t \quad (4)$$

where

$$f = \frac{r_{t+\Delta t}}{r_t} = 1 + \frac{r_{t+\Delta t} - r_t}{r_t} = 1 + \frac{\Delta t}{r_t} \frac{\partial r}{\partial t} \quad (5)$$

Δt refers to the time interval between the simulated time steps. For this study, each cardiac cycle was split into 400 time steps (i.e., $\Delta t = T/400$) in the simulations. The non-Newtonian viscosity of blood used in the simulations follows the Carreau model,

$$\eta = \eta_\infty + (\eta_0 - \eta_\infty) \left[1 + (\lambda\gamma)^2 \right]^{\frac{n-1}{2}} \quad (6)$$

where γ refers to the shear rate, η_∞ is the viscosity for a Newtonian model, 0.0035 Pa s, η_0 is the viscosity at zero shear, 0.056 Pa s, and λ and n are constants equivalent to 3.313 s and 0.3568, respectively.

The boundary conditions were set such that during diastole, the mass flow rate through the mitral valve opening was 0 kg/s, and the pressure at the LVOT was 0 Pa, and during systole, the pressure at the mitral valve opening was 0 Pa and the mass flow rate of LVOT was 0 kg/s. The simulations were conducted for four full cardiac cycles to eliminate transient flows in the results. The details of the simulated hearts can be found in Table 1.

Table 1 Properties of the fetal hearts and their simulation models

	I	II	III
Heart rate (bpm)	147	147	156
End diastolic volume (mm ³)	584	713	886
End systolic volume (mm ³)	146	188	150
Ejection fraction (%)	75.0	73.6	83.1
Diameter of mitral valve opening (mm)	5.0	3.9	4.6
Diameter of aorta (mm)	3.0	4.6	3.1
Mesh elements	1,190,000	1,330,000	1,390,000

3 Results

3.1 Time-resolved motion of fetal left ventricle

Figure 2 shows an example of the echo four-chamber view of the fetal left ventricle (indicated by the white arrow at $t = 0T$) at different times within a cardiac cycle, along with the corresponding 3D model reconstructions (using VMTK) and simulated computational meshes (using ANSYS FLU-ENT 15.0). It can be observed from Fig. 2 that the simulated motion of the fetal left ventricle wall is reasonably close to that indicated by the 3D reconstructed models. This is because the reliability of the simulated ventricle motion is largely dependent on the accuracy of the polynomial fitting for α, θ, ϕ (see Eqs. 4 and 5). Since the R^2 value of the polynomial fitting for Case III shown in Fig. 2 is 0.82, which is considerably precise, it is expected that the simulations followed the motion derived from the 3D reconstructed models sufficiently well. The R^2 values for Cases I and II are 0.74 and 0.82, respectively, implying that the simulated wall motion in these cases are also sufficiently accurate reflections of actual in vivo movement of the fetal ventricle.

Further examining the α versus θ, ϕ plots reveals two distinct peaks for each case, indicating that there were regions of the ventricle wall that exhibited greater oscillatory motion, with respect to the original end systolic centroid, than others (Fig. 3a). These regions are schematically shown in Fig. 3b, highlighted in red. It can be readily observed that they mainly lie in the posterolateral part of the ventricle wall, that is, the part of the wall furthest from the LVOT. This is to be expected, as the parts of the ventricle proximal to the LVOT are also close to the rigid interventricular septum which would have restricted excessive motion. Therefore, this observation provides additional support for the modeling of the ventricular motion.

3.2 Pressure distribution

The dynamic motion of the left ventricle has a direct effect on the pressure distribution of the intraventricular blood flow

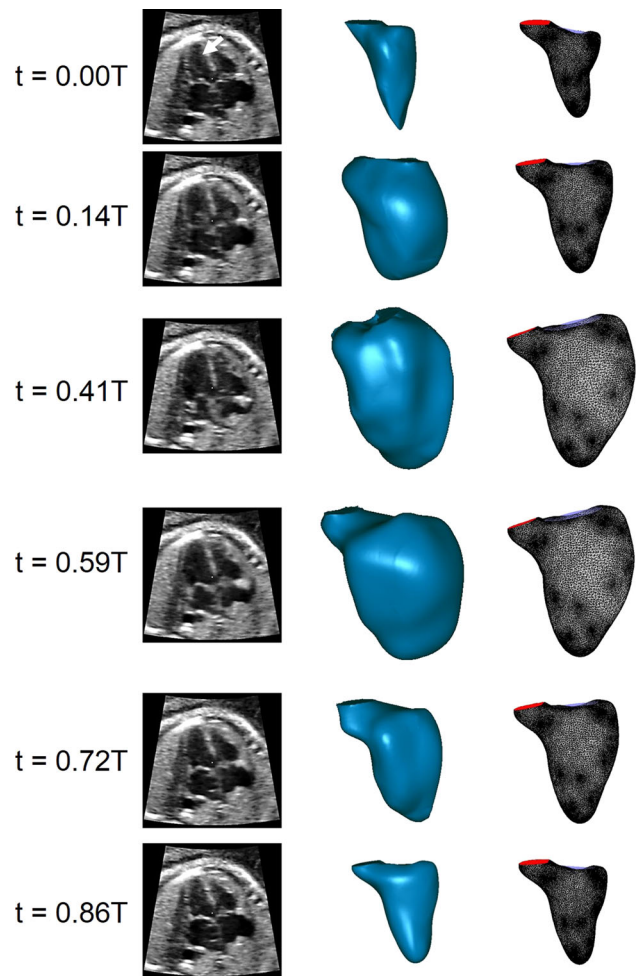
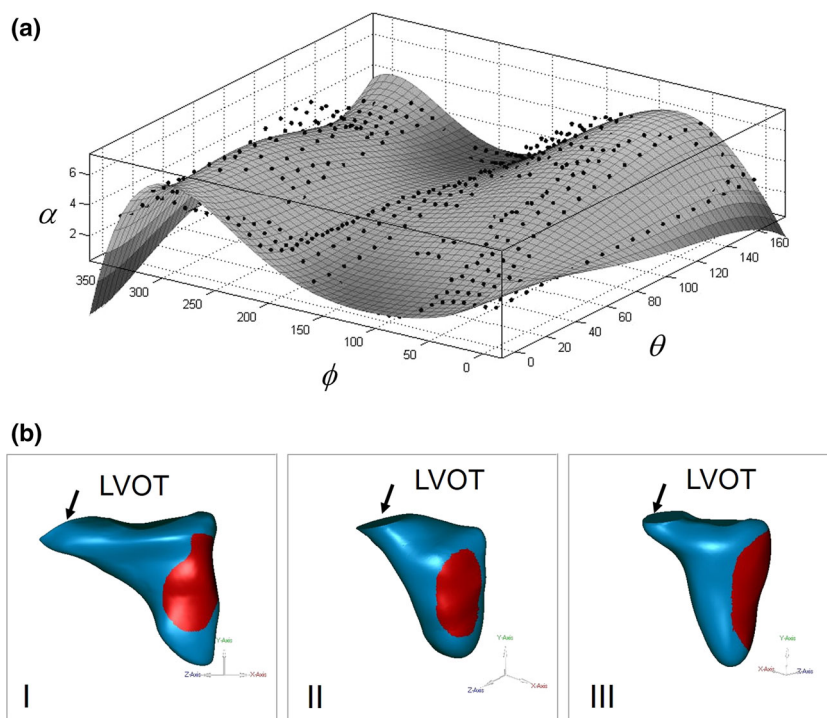


Fig. 2 Ultrasonic four-chamber view (first column), 3D surface reconstruction (second column) and simulated mesh (third column) of a fetal left ventricle over time. The left ventricle is indicated by a white arrow in the ultrasound image at $t = 0T$. T refers to the period of one cardiac cycle

as shown in Fig. 4. Note that the values in the figure do not represent absolute pressure. Instead, they refer to the spatial variation of pressure at various parts of the cardiac cycle, using the pressure at the inlet and outlet boundaries as references during diastole and systole, respectively. This corresponds to the pressure necessary to cause the accelerations and decelerations of fluid over the cardiac cycle and is an indication of the amount of energy that is expended to bring about the filling and draining of the ventricle.

Across the three subjects studied, the average atrium–ventricle pressure difference at peak diastole is 392 ± 344 Pa (2.94 ± 2.58 mmHg) and the average ventricle–aorta pressure difference at peak systole is 383 ± 314 Pa (2.87 ± 2.36 mmHg). The diastolic pressure drop from atrium to ventricle is similar to the values reported previously for fetal hearts of 20-week gestational age (Johnson et al. 2000). In addition, the pressure drop between the ventricle and the

Fig. 3 **a** Surface fitting of α versus θ and ϕ . **b** Schematic of the three fetal hearts, with areas with higher amplitudes of movement highlighted in red



outflow tract was approximately 10% of fetal peak systolic pressure (Johnson et al. 2000). This is similar to but slightly higher than that in an adult left ventricle, which is approximately 5% of peak systolic pressure (Paspoularides et al. 1987).

During the early diastolic E-wave and A-wave, the pressure in the basal region surrounding the mitral valve opening can be seen to be lower than the other regions of the ventricle. This is most likely the Bernoulli's effects of the higher velocity of inflow, which causes fluid entrainment from these basal regions, thus reducing their pressure (Fig. 4). The large discrepancy between velocities of inflow and that of surrounding fluid resulted in high fluid shear stresses, which in turn, brought about vorticity around the inflow fluid column, causing the formation of the vortex ring. The vortex ring allows a conservation of kinetic energy in diastolic ventricular flows near to the center of the ventricular chamber, and since the vortex ring did not dissipate before the ejection phase, some of the kinetic energy conserved from the mitral inflow contributed to the kinetic energy of outflow. Toward the end of diastole, with the decrease in inflow, the pressure distribution along the ventricular wall became more homogenized (Fig. 4, $t = 0.50T$).

During early systole, higher-pressure gradients were encountered because of the rapid acceleration of fluid toward the outflow tract. The apical region had the greatest relative pressure since it was furthest away from the LVOT, and every point on the ventricular wall was contracting simultaneously. As systole progressed, the free, posterolateral wall began to

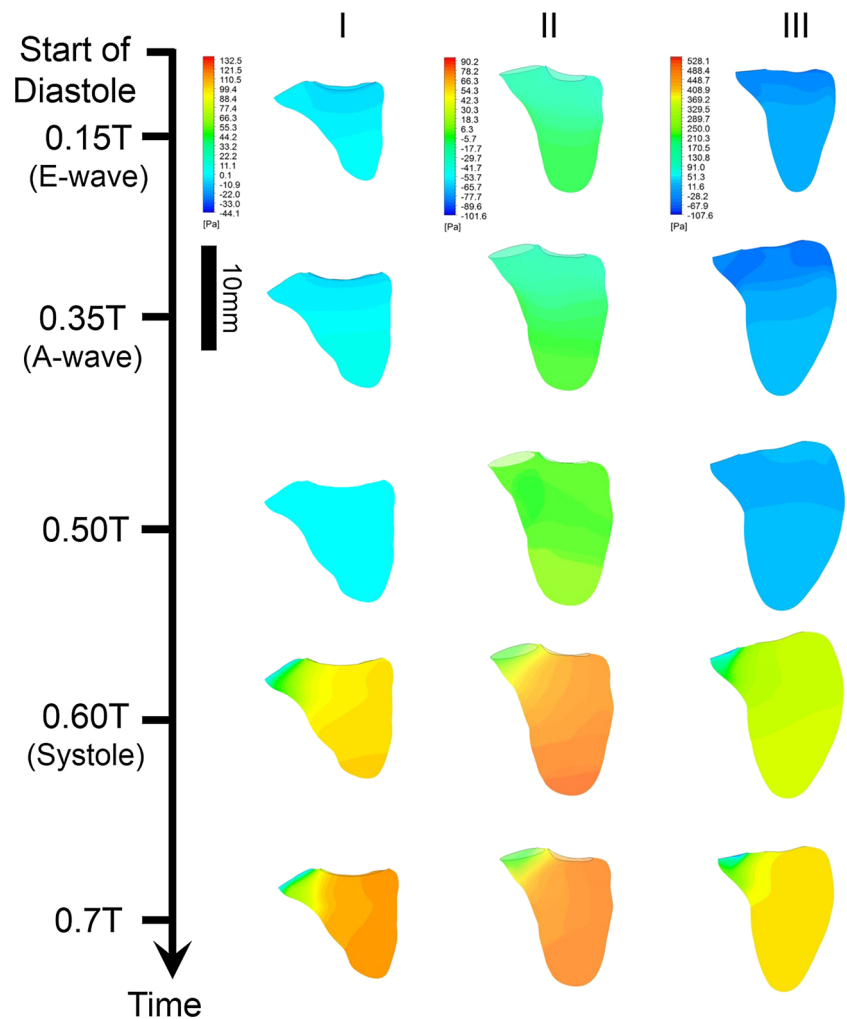
contract more strongly (as discussed in the previous section), and the pressure on the wall increased to the same level as the apical region. The buildup of pressure in the posterolateral wall and apical region was important to ensure that flow is going in the right direction and that there was efficient transfer of energy from the ventricular walls to the blood ejected through the LVOT.

3.3 Streamlines

Figure 5 shows the streamlines of the fetal intraventricular flow. The average peak flow velocities across the three subjects were found to be 0.20 ± 0.09 m/s (E-wave), 0.22 ± 0.11 (A-wave) and 0.52 ± 0.31 (systole), which are reasonably close to the range of measured flow velocities (Groeneweg et al. 1990; Tulzer et al. 1994). The simulated values are generally on the lower end of the spectrum, however, possibly due to inaccuracies in the simulated motion causing slight expansions of the mitral valve opening and LVOT, which in turn, led to a lowering of flow velocities.

It can also be observed that during the diastolic E-wave and A-wave acceleration, the blood flowed from the left atrium to the left ventricle through the mitral valve opening at high velocities. Due to the flow separation and subsequently, high shear between the inflow fluid column and its surrounding fluid, vortex rings were observed to form. The rest of the streamlines not involved in vortex formation slowed down as they approached the apical region due to the buildup of

Fig. 4 Pressure distribution on the left fetal ventricular wall over time for Cases I, II and III. Note that the value of the pressure indicated here is relative to that of the inlet during systole and outlet during diastole and corresponds to the pressure difference necessary to drive the observed blood flow in the ventricle



pressure at the mid and apical regions of the ventricle (Fig. 4, $t = 0.15T$ and $0.35T$).

During systole, the streamlines had the greatest velocities at the LVOT as the positive wall pressures accelerated the fluid toward the outflow tract (Fig. 4). Physically, the ejection of the blood during systole was observed to be achieved through both the lateral squeezing of the posterolateral walls and the shortening of the left ventricle along the longitudinal axis.

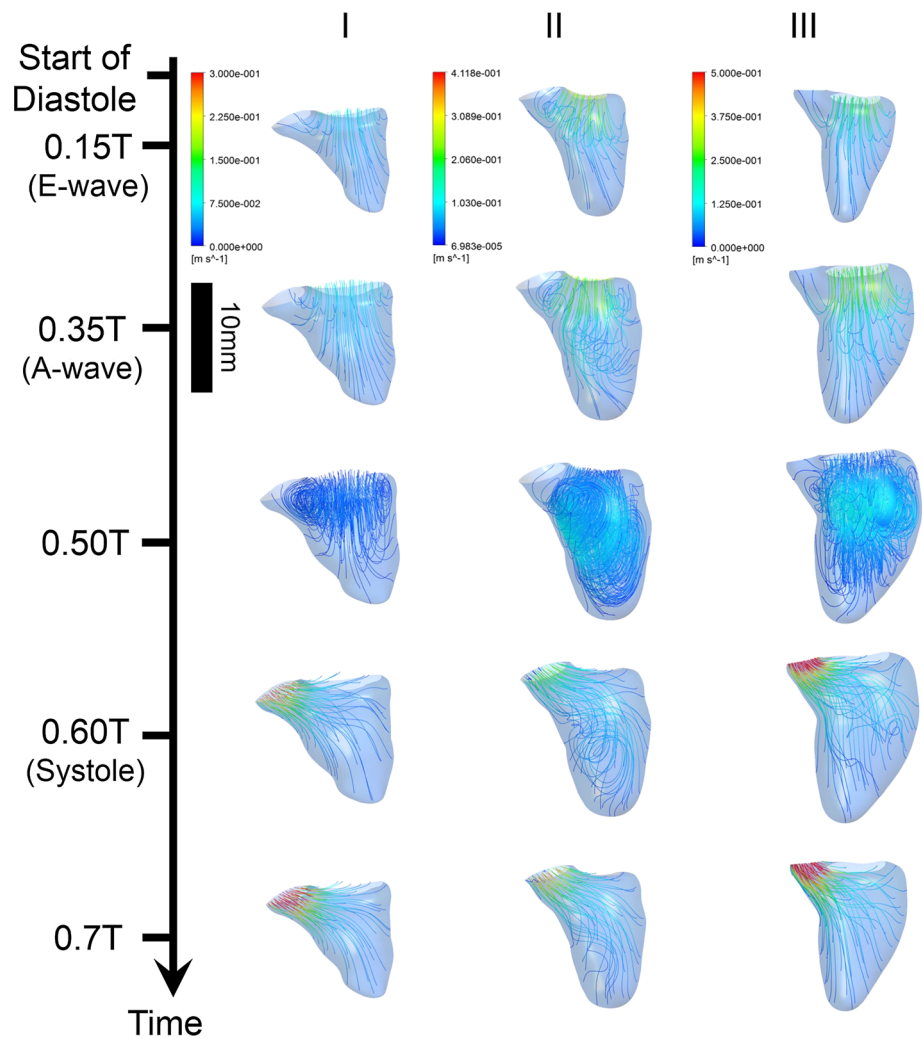
3.4 Vortex formation

The complex patterns of the streamlines shown in Fig. 5 can be better described in terms of isosurfaces of vortex cores using the well-established lambda-2 criterion (Jeong and Hussain 1995; Fig. 6). The flow around these vortex cores can be visualized with 2D velocity curl (colored contours) and in-plane velocity vectors (black arrows) plotted on a 2D plane that cuts through the middle of the LVOT and mitral valve opening as shown in Fig. 7.

From Fig. 6, it can be seen that the diastolic E-wave and A-wave each generated a toroidal (ring-shaped) vortex core, an observation that was also previously made with adult left ventricles (Elaz et al. 2014). On a 2D plane, the toroidal vortex core appears as two counter-rotating vortices (Fig. 7; Heiberg et al. 2003). Each time after the vortex was sufficiently formed and gathered sufficient momentum, it detached itself from the mitral valve opening and migrated downwards toward the midsection of the ventricle. Upon detachment, the primary vortex ring interacts with the basal region of the ventricular wall, leading to the formation of secondary vortices which wrapped themselves around the primary ring (Le and Sotiropoulos 2012), one example of which is indicated with the red arrow in Fig. 6.

More importantly, during the course of its downward movement, the toroidal vortex core interacted with the posterolateral and anteroseptal ventricle walls (left and right walls of the ventricles shown in Fig. 7). This caused the relevant sections of the toroidal vortex core to weaken and break up into smaller secondary vortices (black arrow in Fig. 7), disappearing from the isosurface plot and leaving only two

Fig. 5 Streamline distribution in the fetal left ventricle over time for Cases I, II and III



branches of vortex cores in the mid-anterolateral and mid-posteroseptal regions intact (with respect to the view shown in Case I in Fig. 6, these regions correspond to the back-side and front side of the ventricle respectively). These two branches of vortex cores were then observed to be ejected through the LVOT during systole (Fig. 6, $t = 0.6T$ and $t = 0.75T$).

The presence of the two counter-rotating vortex cores in the systolic outflow implies that the flow entering the fetal aorta would be double helical. This was confirmed by plotting the in-plane velocity vectors and 2D velocity curl at the LVOT, as shown in Fig. 8. In Cases I and II, the left-handed helical flows were dissipated faster, which caused the blood to be ejected with a predominantly right-handed helical flow. In Case III, however, the dissipation rate of the right-handed and left-handed helical flows were similarly slow, and thus, the systolic outflow was ejected with two counter-rotating in-plane vortices. Note that a counterclockwise curl observed in Fig. 8 would mean a right-handed helical flow in the fetal aorta.

Previous work have shown that flow through the aorta may manifest as a double-helical flow or a single-helical flow due to the curved geometry of the aorta (Kilner et al. 1993; Yap et al. 2014), depending on the Germano and Dean numbers (Liu and Masliyah 1993). Our results, indicated that, in the fetus, helicity is already established in the flow entering the aorta. Moreover, the maximum in-plane velocity in the systolic outflow is of the same order of magnitude as that of the maximum axial velocity, suggesting a highly intense helicity, which should have significant influence on the aortic flow.

3.5 Wall shear stress

Figure 9 shows the wall shear stress (WSS) distribution on the ventricular walls. It can be readily observed in all three cases that during diastole, a band of high WSS was constantly in the vicinity of the toroidal vortices, mimicking their migration toward the mid and apical regions. This observation can be explained by the high velocity intensities around the vortex cores, fueled by remnant momentum from the inflow.

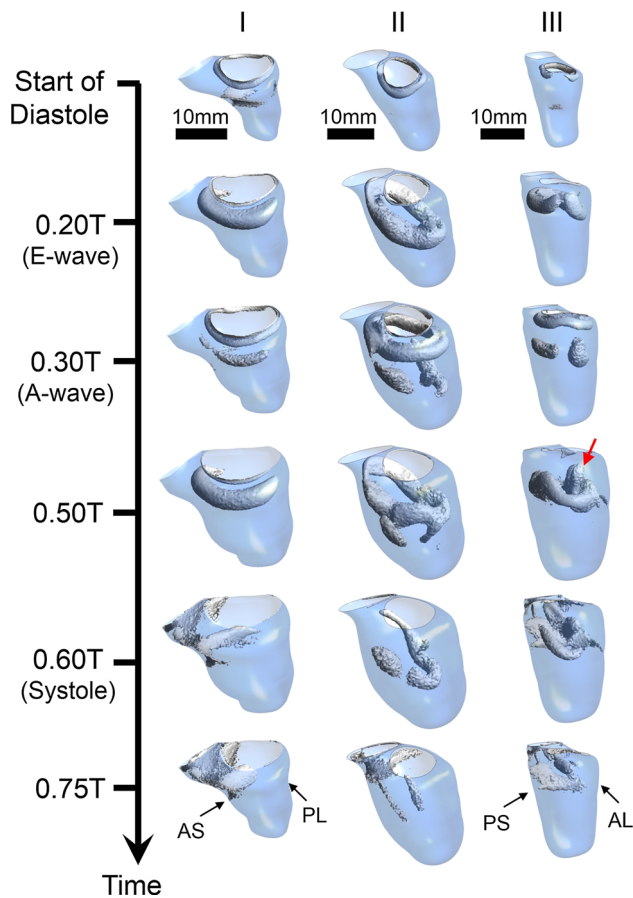


Fig. 6 Isosurfaces of vortex rings formed in the fetal left ventricles using the lambda-2 criterion. The red arrow points to a secondary vortex formed due to the interaction of the main toroidal vortex with the ventricular walls. AS, PL, PS and AL refer to the anteroseptal, posterolateral, posteroseptal and anterolateral faces of the fetal left ventricles, and their positions are indicated with the models shown for $t = 0.75T$

As the vortex core approached the ventricular walls, these velocities became tangential to the wall (Fig. 5), thus generating high WSS (peak WSS = 0.5–5 Pa). In contrast, for the non-vortical regions, such as the apical section, low levels of WSS were found (Fig. 9). This can be explained by the observations that the flow in these regions had low velocities and flow directions that were mostly normal to the ventricular wall (Fig. 5). During systole, the highest WSS were located at the walls of LVOT, which is expected because of the high velocities that the blood were being ejected with.

4 Discussion

We highlight that the fluid mechanics results in the current studies are results of flow simulations, and not directly measured from ultrasound imaging. It is currently unclear to what extent the ventricular vortex rings are formed in fetal hearts,

and future work are warranted, especially direct imaging studies.

4.1 Comparison between fetal and adult left ventricles

There are at least three main differences between the left ventricular motion of a fetal and adult heart. The first dissimilarity arises because of their difference in the diastolic E/A ratio. For a normal adult ventricle, the peak E-wave to peak A-wave velocity ratio lies in the range of 0.75–1.5 (Markl et al. 2005). In contrast, for a fetal heart with a gestational age of 20 weeks, the peak E-wave is only 0.6 times that of the peak A-wave velocity (Chang et al. 2000). This is directly reflected by the rate at which the ventricle expands during diastole, so that a fetal ventricle enlarges much faster during the A-wave than E-wave, while the reverse is true for an adult heart.

The second dissimilarity is the higher heart rate of a normal fetal heart (~ 150 bpm) as compared to a normal adult heart (~ 70 bpm; Bombardini et al. 2008), meaning that the motion of a fetal heart is approximately twice as frequently as that of an adult heart. Lastly, the systole–diastole duration ratio is different for the fetal left ventricle (~ 0.5) and adult left ventricle (~ 0.7) (Bombardini et al. 2008).

Owing to these disparities in their ventricular wall motion, the mechanics of intraventricular flow are generally different for fetal and adult ventricles. For instance, in adult left ventricles, the period between the onset of E- and A-wave during diastole is longer, allowing the E-wave vortex ring to break up much more significantly before the formation of the A-wave vortex ring (Elaz et al. 2014). In addition, for an adult left ventricle, the anteroseptal section (the side near to the LVOT) of the vortex ring tends to be preserved to the end of diastole rather than the anterolateral and posteroseptal branches of the vortex ring (Fig. 6). Because of these differences, the fetal systolic outflow helicity is under a stronger influence of ventricular vortex flows than that in the adult, as more vertical structures are preserved and ejected.

Just as the motion of a fetal left ventricle is not completely different from that of an adult left ventricle (e.g., both ventricles basically go through diastolic and systolic phases), there can be some similarities between the intraventricular flows of a fetal and adult heart too. Firstly, a vortex ring is generated for the E-wave as well as for the A-wave during diastole (Elaz et al. 2014). In addition, for both adult and fetal left ventricles, the vortex rings were seen to migrate toward the apical section and interactions with the ventricular wall produces secondary vortex tubes that wrap themselves around the main vortex rings (Elaz et al. 2014; Le and Sotiropoulos 2012). Finally, upon striking the posterolateral ventricular wall, the affected section of the vortex ring tend to break up into multiple smaller vortices (Le and Sotiropoulos 2012).

Fig. 7 Contour maps of 2D curl and in-plane velocity vectors in the middle of the fetal left ventricles. *Black arrow* points to the breakup of a vortex into two smaller vortices upon striking the ventricular wall

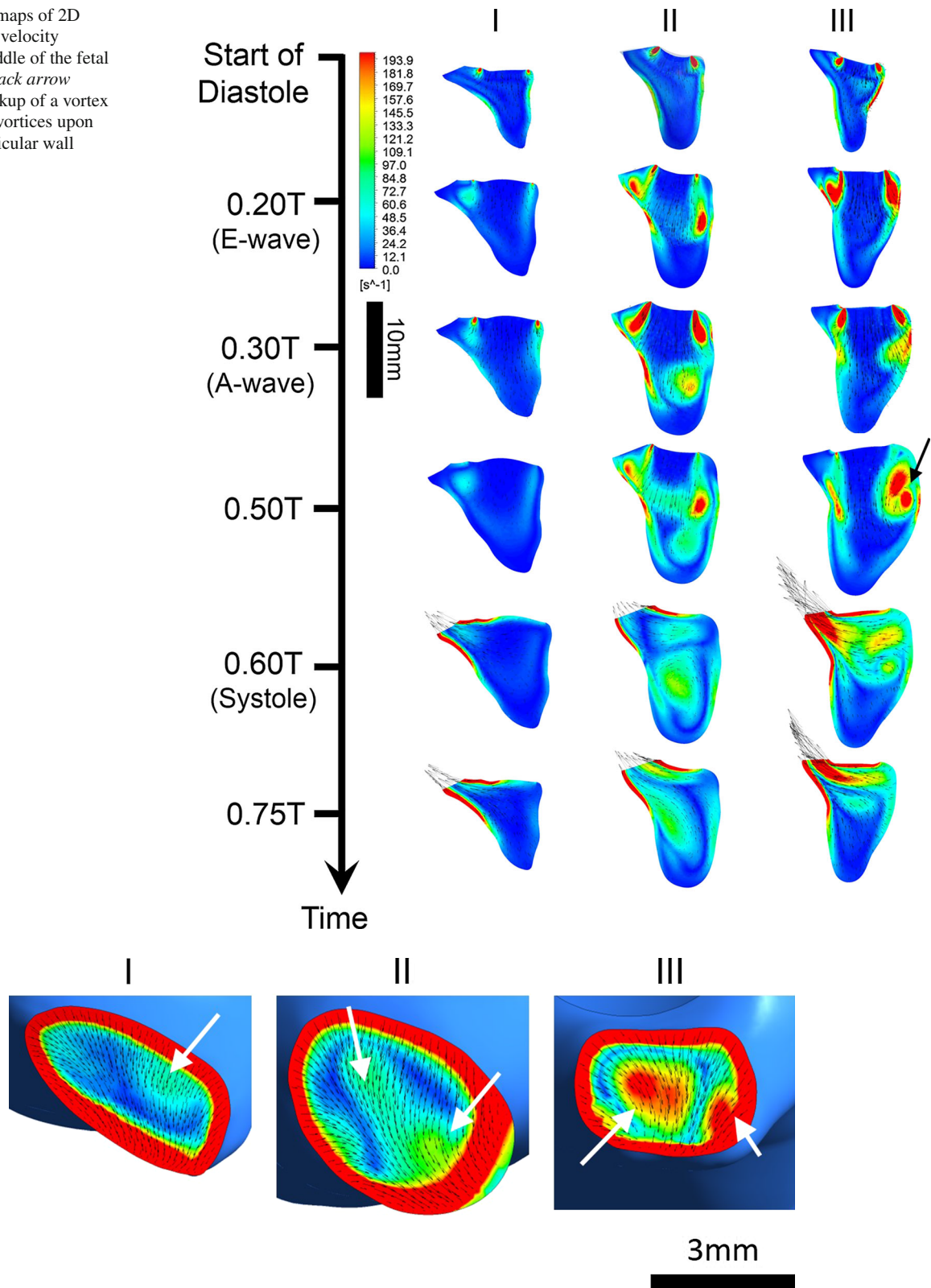
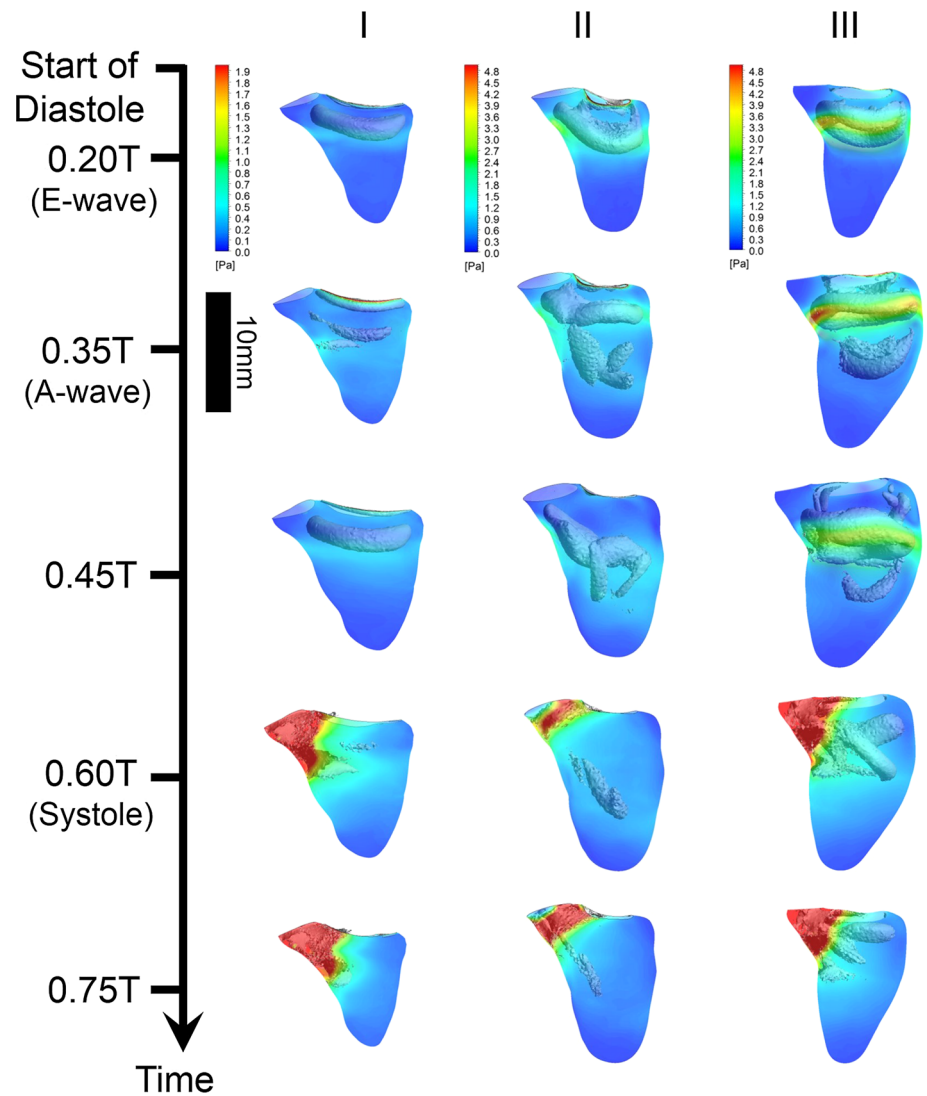


Fig. 8 Contour maps of 2D curl and in-plane velocity vectors at the LVOT. *White arrows* point to the center of the vortices. The axial flow direction is toward the reader. Therefore, a clockwise in-plane velocity indicates a right-handed helical flow

Fig. 9 Wall shear stress distribution in the left fetal ventricular wall and the isosurfaces of vortex rings plotted with the lambda-2 criterion



4.2 Effects of vortex formation: low pressure

Vortex formation in human hearts have been the subject of many studies and have been suggested as a clinical index for assessing the cardiac health of patients (Elaz et al. 2014). The creation of the vortices conserves the kinetic energy of the blood (the velocity of the streamlines are highest in the vortical regions as shown in Fig. 5) entering through the mitral valve opening during diastole. Via Bernoulli’s effects, this avoids the conversion of kinetic energy to pressure, thus maintaining a slightly lower pressure region with respect to the left atrium (Pasipoularides 2013), which may play a role in reducing the energy expenditure during the heart’s pumping (Martínez-Legazpi et al. 2014).

4.3 Effects of vortex formation: high shear stresses

On the other hand, the high kinetic energy of the flow in the vortices leads to high WSS, which had previously been identified as an important epigenetic factor that can bring about changes to cardiac physiology and function (Davies et al. 1986; Fry 1968; Hove et al. 2003; Olesen et al. 1988). To accomplish this, the WSS provides mechanical feedback through the endothelial cells to influence the regulation of genes (WSS ~ 0.1 Pa) (Olesen et al. 1988) or alter the cytoskeletal structure of the cells directly (WSS ~ 1 Pa) (Davies et al. 1986; Raz et al. 2005). Beyond 38 Pa, however, the endothelium will be eroded, impairing the shear-sensing ability of the ventricle (Fry 1968). Since the vortex-induced

WSS in the fetal ventricles ranges from 1 to 4 Pa (Fig. 9), it is more than likely to be involved in some regulatory role, especially in the orderly alignment of the cardiac muscle cells found in normal fetal hearts (Maron et al. 1979).

The support for this premise comes from previous studies on hypoplastic left heart syndrome (HLHS), where the left ventricle failed to develop at the same rate as the right ventricle, and was too small to be functional at birth. The lack of flow into the left ventricle is widely hypothesized to be the cause of HLHS, either from the inability of the foramen ovale to sustain inflow (Mäkikallio et al. 2006) or from the aortic outflow obstruction (Tworetzky et al. 2004). This reduced flow in the left ventricle, the consequently reduced shear stress, and lack of shear stimulated growth of the left ventricle is a likely mechanism by which the HLHS develops during fetal stages. Conversely, the presence of vortex-induced WSS may be an important stimuli for sustained growth of the left ventricle. In fact, recent novel fetal surgery relieving the outflow tract obstruction was shown to be able to enhance the left ventricle's growth to avoid single ventricle presentations at birth (Tworetzky et al. 2004). Furthermore, the similarity between the values of the vortex-induced WSS in fetal (Fig. 9) and adult ventricles (Pasipoularides 2012) may suggest that a WSS homeostasis may exist between fetal and adult lives, where any elevation in WSS would cause a corresponding growth in the ventricle so as to restore WSS to a homeostatic level, thereby allowing WSS to control the growth of the ventricle.

In the case of hypertrophic cardiomyopathy, the left ventricle contains approximately 100 times larger areas of disorganized muscle cells than normal ventricles (Maron et al. 1981, 1979). In addition, hypertrophic cardiomyopathic left ventricles were also found to have significantly reduced vortex formation, as the overgrowth of the ventricular walls resulted in a much narrower ventricular chamber (Martínez-Legazpi et al. 2014). We hypothesize that the attenuation of vortex-induced WSS in hypertrophic cardiomyopathic ventricles could be the driving cause for the disorganized growth of cardiac muscle cells, since previous studies have shown that shear stresses in the order of 1 Pa are known to align endothelial cells to the flow (Davies et al. 1986). Despite strong evidence that the initiation of hypertrophic cardiomyopathy and cell disorganization is due to genetic mutations affecting myosin proteins, and impairing cardiac myocyte function (Chung et al. 2003; Marian et al. 2001; Pagon et al. 2014; Yang et al. 1998), our hypothesized mechanics pathway may play a role in the progression of the disease.

4.4 Effects of vortex formation: helical flow in fetal aorta

It had previously been suggested that the diastolic ventricular vortex rings to have the role of conserving momentum energy

for use during systolic outflow (Duran et al. 2013; Pedrizzetti and Domenichini 2014). The results of our study appear to support this, as ventricular vortices were shown to be preserved from the diastolic to systolic phase, and were directly responsible for the helical flows generated at the LVOT during systole (Fig. 6). The energetics of these vortical structures will be investigated in detail in future studies and compared to that found in adult hearts.

5 Limitations

The main limitation in this present study is the absence of other important physiological features such as mitral valves, papillary muscles, chordae tendineae, and trabeculations in our ventricular model and simulations. Nevertheless, despite omitting such features, previous simulation studies have shown important results that were validated with experimental observations and measurements (Fortini et al. 2013; Le and Sotiropoulos 2012), and hence, the insights derived from this study are still expected to be useful.

Secondly, our choice of using the ultrasound as the scanning modality comes with issues of increased noise level, and limited resolution, compared to other modalities such as MRI and CT. However, as discussed above, ultrasound is the only feasible approach for human fetuses currently. Due to noise and resolution issues, we were unable to retrieve fine details of E- and A-wave wall motions from segmentation of the images, even when we segmented images at all time points. We had thus relied on pulse-wave measurements of mitral inflow and aortic outflow from the literature to guide our wall motion model. The segmentations were only used for curve-fitting to compute amplitudes of wall motion, and thus segmentations at fewer time points were used.

Our future work will focus on increasing the biological accuracy of the models and improving the temporal resolution of the technique, using patient-specific data, such as flow velocity measurements, to validate our simulation results. However, these shortcomings are not expected to significantly alter the general conclusions of our present work at this point.

6 Conclusions

The present study demonstrated a technique for carrying out CFD simulations of blood flow in a fetal left ventricle by quantifying the motion of the ventricle observed in 4D STIC ultrasound scans. It was found from the simulations that the fetal left ventricular motion is dissimilar to that of an adult ventricle, but nevertheless, leads to some general similarities in the results of their flow simulations. In addition, vortex formation in the fetal left ventricle was described in detail and shown to produce low pressure regions, high wall shear

stress and initiate helical flow in the fetal aorta. The low pressure generated by the vortices were expected to improve the efficiency of diastolic filling while WSS was suggested as an epigenetic factor for aligning the cardiac cells in normal fetal hearts.

Acknowledgments The authors would like to thank Singapore Ministry of Health, National Medical Research Council Grant Number NMRC/BNIG/2020/2014 (PI: Yap) for funding.

References

- Ahmed BI (2014) The new 3D/4D based spatio-temporal imaging correlation (STIC) in fetal echocardiography: a promising tool for the future. *J Matern Fetal Neonatal Med* 27:1163–1168
- Bellhouse B (1972) Fluid mechanics of a model mitral valve and left ventricle. *Cardiovasc Res* 6:199–210
- Bombardini T et al (2008) Diastolic time-frequency relation in the stress echo lab: filling timing and flow at different heart rates. *Cardiovasc Ultrasound* 6:15
- Chang C-H, Chang F-M, Yu C-H, Liang R-I, Ko H-C, Chen H-Y (2000) Systemic assessment of fetal hemodynamics by Doppler ultrasound. *Ultrasound Med Biol* 26:777–785
- Chung M-W, Tsoutsman T, Semsarian C (2003) Hypertrophic cardiomyopathy: from gene defect to clinical disease. *Cell Res* 13:9–20
- Davies PF, Remuzzi A, Gordon EJ, Dewey CF, Gimbrone MA (1986) Turbulent fluid shear stress induces vascular endothelial cell turnover in vitro. *Proc Natl Acad Sci* 83:2114–2117
- DeVore G, Falkensammer P, Sklansky M, Platt L (2003) Spatio-temporal image correlation (STIC): new technology for evaluation of the fetal heart. *Ultrasound Obstet Gynecol* 22:380–387
- Duran C, Angell WW, Johnson AD (2013) Recent progress in mitral valve disease. Elsevier, Amsterdam
- Elaz MS, Calkoen EE, Westenbergh JJ, Lelieveldt BP, Roest AA, van der Geest RJ (2014) Vortex flow during early and late left ventricular filling in normal subjects: quantitative characterization using retrospectively-gated 4D flow cardiovascular magnetic resonance and three-dimensional vortex core analysis. *J Cardiovasc Magn Reson* 16:78
- Fortini S, Querzoli G, Espa S, Cenedese A (2013) Three-dimensional structure of the flow inside the left ventricle of the human heart. *Exp Fluids* 54:1–9
- Fry DL (1968) Acute vascular endothelial changes associated with increased blood velocity gradients. *Circ Res* 22:165–197
- Ghosh E, Shmuylovich L, Kovács SJ (2010) Vortex formation time-to-left ventricular early rapid filling relation: model-based prediction with echocardiographic validation. *J Appl Physiol* 109:1812–1819
- Godfrey M, Messing B, Cohen S, Valsky D, Yagel S (2012) Functional assessment of the fetal heart: a review. *Ultrasound Obstet Gynecol* 39:131–144
- Groenenberg I, Stijnen T, Wladimiroff J (1990) Blood flow velocity waveforms in the fetal cardiac outflow tract as a measure of fetal well-being in intrauterine growth retardation. *Pediatr Res* 27:379–382
- Groenendijk BC, Hierck BP, Vrolijk J, Baiker M, Pourquie MJ, Gittenberger-de Groot AC, Poelmann RE (2005) Changes in shear stress-related gene expression after experimentally altered venous return in the chicken embryo. *Circ Res* 96:1291–1298
- Heiberg E, Ebberts T, Wigström L, Karlsson M (2003) Three-dimensional flow characterization using vector pattern matching. *IEEE Trans Vis Comput Graph* 9:313–319
- Hogers B, DeRuiter M, Baasten A, Gittenberger-de Groot A, Poelmann R (1995) Intracardiac blood flow patterns related to the yolk sac circulation of the chick embryo. *Circ Res* 76:871–877
- Holmes WM, McCabe C, Mullin JM, Condon B, Bain MM (2008) Noninvasive self-gated magnetic resonance cardiac imaging of developing chick embryos in ovo. *Circulation* 117:e346–e347
- Hove JR, Köster RW, Forouhar AS, Acevedo-Bolton G, Fraser SE, Gharib M (2003) Intracardiac fluid forces are an essential epigenetic factor for embryonic cardiogenesis. *Nature* 421:172–177
- Jeong J, Hussain F (1995) On the identification of a vortex. *J Fluid Mech* 285:69–94
- Johnson BM, Garrity DM, Dasi LP (2013) Quantifying function in the early embryonic heart. *J Biomechan Eng* 135:041006
- Johnson P, Maxwell D, Tynan M, Allan L (2000) Intracardiac pressures in the human fetus. *Heart* 84:59–63
- Kilner PJ, Yang GZ, Mohiaddin RH, Firmin DN, Longmore DB (1993) Helical and retrograde secondary flow patterns in the aortic arch studied by three-directional magnetic resonance velocity mapping. *Circulation* 88:2235–2247
- Le TB, Sotiropoulos F (2012) On the three-dimensional vortical structure of early diastolic flow in a patient-specific left ventricle. *Eur J Mech B Fluids* 35:20–24
- Liu S, Masliyah JH (1993) Axially invariant laminar flow in helical pipes with a finite pitch. *J Fluid Mech* 251:315–353
- Mäkikallio K et al (2006) Fetal Aortic valve stenosis and the evolution of hypoplastic left heart syndrome patient selection for fetal intervention. *Circulation* 113:1401–1405
- Marian A, Salek L, Lutucuta S (2001) Molecular genetics and pathogenesis of hypertrophic cardiomyopathy. *Minerva medica* 92:435
- Markl M et al (2005) Time-resolved three-dimensional magnetic resonance velocity mapping of aortic flow in healthy volunteers and patients after valve-sparing aortic root replacement. *J Thorac Cardiovasc Surg* 130:456–463
- Maron BJ, Anan TJ, Roberts WC (1981) Quantitative analysis of the distribution of cardiac muscle cell disorganization in the left ventricular wall of patients with hypertrophic cardiomyopathy. *Circulation* 63:882–894
- Maron BJ, Sato N, Roberts WC, Edwards JE, Chandra RS (1979) Quantitative analysis of cardiac muscle cell disorganization in the ventricular septum. Comparison of fetuses and infants with and without congenital heart disease and patients with hypertrophic cardiomyopathy. *Circulation* 60:685–696
- Marshall AC et al (2004) Creation of an atrial septal defect in utero for fetuses with hypoplastic left heart syndrome and intact or highly restrictive atrial septum. *Circulation* 110:253–258
- Martínez-Legazpi P et al (2014) Contribution of the diastolic vortex ring to left ventricular filling. *J Am Coll Cardiol* 64:1711–1721
- Olesen S-P, Clapham D, Davies P (1988) Haemodynamic shear stress activates a K⁺ current in vascular endothelial cells. *Nature* 331:168–170
- Pagon RA et al (2014) Hypertrophic cardiomyopathy overview
- Pasipoularides A (2009) Heart's vortex: intracardiac blood flow phenomena. PMPH-USA
- Pasipoularides A (2012) Diastolic filling vortex forces and cardiac adaptations: probing the epigenetic nexus. *Hellenic J Cardiol* 53:458–469
- Pasipoularides A (2013) Evaluation of right and left ventricular diastolic filling. *J Cardiovasc Transl Res* 6:623–639
- Pasipoularides A, Murgo JP, Miller JW, Craig WE (1987) Nonobstructive left ventricular ejection pressure gradients in man. *Circ Res* 61:220–227
- Pedrizetti G, Domenichini F (2014) Left ventricular fluid mechanics: the long way from theoretical models to clinical applications. *Ann Biomed Eng* 43:26–40

- Raz D, Zaretsky U, Einav S, Elad D (2005) Cellular alterations in cultured endothelial cells exposed to therapeutic ultrasound irradiation. *Endothelium* 12:201–213
- Taddei F, Franceschetti L, Signorelli M, Prefumo F, Fratelli N, Frusca T, Grolì C (2007) Spatio-Temporal Imaging Correlation (STIC) in fetal echocardiography
- Tobita K, Keller BB (2000) Right and left ventricular wall deformation patterns in normal and left heart hypoplasia chick embryos. *Am J Physiol Heart Circ Physiol* 279:H959–H969
- Tulzer G, Khowsathit P, Gudmundsson S, Wood DC, Tian Z-Y, Schmitt K, Huhta JC (1994) Diastolic function of the fetal heart during second and third trimester: a prospective longitudinal Doppler-echocardiographic study. *Eur J Pediatr* 153:151–154
- Tworetzky W et al (2004) Balloon dilation of severe aortic stenosis in the fetus potential for prevention of hypoplastic Left Heart Syndrome: Candidate selection technique, and results of successful intervention. *Circulation* 110:2125–2131
- Wang Y, Dur O, Patrick MJ, Tinney JP, Tobita K, Keller BB, Pekkan K (2009) Aortic arch morphogenesis and flow modeling in the chick embryo. *Ann Biomed Eng* 37:1069–1081
- Wigström L, Ebbers T, Fyrenius A, Karlsson M, Engvall J, Wranne B, Bolger AF (1999) Particle trace visualization of intracardiac flow using time-resolved 3D phase contrast MRI. *Magn Reson Med* 41:793–799
- Yamashita S et al (2007) Visualization of hemodynamics in intracranial arteries using time-resolved three-dimensional phase-contrast MRI. *J Magn Reson Imaging* 25:473–478
- Yang Q, Sanbe A, Osinska H, Hewett TE, Klevitsky R, Robbins J (1998) A mouse model of myosin binding protein C human familial hypertrophic cardiomyopathy. *J Clin Invest* 102:1292
- Yap CH, Liu X, Pekkan K (2014) Characterization of the vessel geometry, flow mechanics and wall shear stress in the great arteries of wildtype prenatal mouse. *PLoS One* 9(1):e86878